X-ray polarimetry of the accreting pulsar GX 301−2

Valery F. Suleimanov[1], Sofia V. Forsblom[2], Sergey S. Tsygankov[2], Juri Poutanen[2], Victor Doroshenko[1],
Rosalia Doroshenko[1], Fiamma Capitanio[3], Alessandro Di Marco[3], Denis González-Caniulef[4], Jeremy Heyl[5],
Fabio La Monaca[3], Alexander A. Lutovinov[6], Sergey V. Molkov[6], Christian Malacaria[7], Alexander A. Mushtukov[8],
Andrey E. Shtykovsky[6, 9], Iván Agudo[10], Lucio A. Antonelli[11, 12], Matteo Bachetti[13], Luca Baldini[14, 15],
Wayne H. Baumgartner[16], Ronaldo Bellazzini[14], Stefano Bianchi[17], Stephen D. Bongiorno[16], Raffaella Bonino[18, 19],
Alessandro Brez[14], Niccolò Bucciantini[20, 21, 22], Simone Castellano[14], Elisabetta Cavazzuti[23], Chien-Ting Chen[24],
Stefano Ciprini[25, 12], Enrico Costa[3], Alessandra De Rosa[3], Ettore Del Monte[3], Laura Di Gesu[23], Niccolò Di Lalla[26],
Immacolata Donnarumma[23], Michal Dovčiak[28], Steven R. Ehlert[16], Teruaki Enoto[29], Yuri Evangelista[3],
Sergio Fabiani[3], Riccardo Ferrazzoli[3], Javier A. Garcia[30], Shuichi Gunji[31], Kiyoshi Hayashida[32][⋆], Wataru Iwakiri[33],
Svetlana G. Jorstad[34, 35], Philip Kaaret[16], Vladimir Karas[28], Fabian Kislat[36], Takao Kitaguchi[29],
Jeffery J. Kolodziejczak[16], Henric Krawczynski[37], Luca Latronico[18], Ioannis Liodakis[38], Simone Maldera[18],
Alberto Manfreda[39], Frédéric Marin[40], Andrea Marinucci[23], Alan P. Marscher[34], Herman L. Marshall[41],
Francesco Massaro[18, 19], Giorgio Matt[17], Ikuyuki Mitsuishi[42], Tsunefumi Mizuno[43], Fabio Muleri[3],
Michela Negro[44, 45, 46], Chi-Yung Ng[47], Stephen L. O'Dell[16], Nicola Omodei[26], Chiara Oppedisano[18],
Alessandro Papitto[11], George G. Pavlov[48], Abel L. Peirson[26], Matteo Perri[12, 11], Melissa Pesce-Rollins[14],
Pierre-Olivier Petrucci[27], Maura Pilia[13], Andrea Possenti[13], Simonetta Puccetti[12], Brian D. Ramsey[16], John Rankin[3],
Ajay Ratheesh[3], Oliver J. Roberts[24], Roger W. Romani[26], Carmelo Sgrò[14], Patrick Slane[49], Paolo Soffitta[3],
Gloria Spandre[14], Douglas A. Swartz[24], Toru Tamagawa[29], Fabrizio Tavecchio[50], Roberto Taverna[51], Yuzuru Tawara[42],
Allyn F. Tennant[16], Nicholas E. Thomas[16], Francesco Tombesi[52, 25, 53], Alessio Trois[13], Roberto Turolla[51, 54],
Jacco Vink[55], Martin C. Weisskopf[16], Kinwah Wu[54], Fei Xie[56, 3], and Silvia Zane[54]

(Affiliations can be found after the references)

May 25, 2023

ABSTRACT

The phase- and energy-resolved polarization measurements of accreting X-ray pulsars (XRPs) allow us to test different theoretical models of their emission, as well as to provide an avenue to determine the emission region geometry. We present the results of the observations of the XRP GX 301−2 performed with the *Imaging X-ray Polarimetry Explorer* (*IXPE*). GX 301−2 is a persistent XRP with one of the longest known spin periods of ∼680 s. A massive hyper-giant companion star Wray 977 supplies mass to the neutron star via powerful stellar winds. We do not detect significant polarization in the phase-averaged data using spectro-polarimetric analysis, with the upper limit on the polarization degree (PD) of 2.3% (99% confidence level). Using the phase-resolved spectro-polarimetric analysis we get a significant detection of polarization (above 99% c.l.) in two out of nine phase bins and marginal detection in three bins, with a PD ranging between ∼3% and ∼10%, and a polarization angle varying in a very wide range from ∼0° to ∼160°. Using the rotating vector model we obtain constraints on the pulsar geometry using both phase-binned and unbinned analysis getting excellent agreement. Finally, we discuss possible reasons for a low observed polarization in GX 301−2.

Key words. magnetic fields – methods: observational –polarization – stars: neutron – X-rays: binaries — X-rays: individual (GX 301−2)

1. Introduction

Accreting X-ray pulsars (XRPs; see Mushtukov & Tsygankov 2022, for a recent review) are highly magnetized neutron stars (NS) with the surface magnetic field strength of 10^{12}–10^{13} G, orbiting early-type (typically O-B) donor stars. The NS accretes matter lost by the donor star through the stellar wind, or decretion disk in the case of Be systems. In some systems, an accretion disk around the NS may also form. The accretion flow in the vicinity of the NS surface is governed by the magnetic field, and the accreting matter forms hotspots near the NS magnetic poles radiating in the X-ray band. There are no commonly accepted models of the radiating regions, however, it is clear that at high enough mass accretion rates, the emitting hotspots transform to radially extended accretion columns (Basko & Sunyaev 1976; Becker et al. 2012; Mushtukov et al. 2015).

Radiation generated by plasma in a strong magnetic field was expected to be highly polarized at the photon energies below the cyclotron energy, because of the birefringence of magnetized plasma (see, e.g., Harding & Lai 2006; Caiazzo & Heyl 2021). Testing these predictions became possible recently thanks to the *Imaging X-ray Polarimetry Explorer* (*IXPE*) that allows one to measure X-ray polarization in the 2–8 keV energy band. In the first year of its operation, *IXPE* has carried out polarization measurements of several XRPs (Her X-1, Doroshenko et al. 2022; Cen X-3, Tsygankov et al. 2022; 4U 1626−67, Marshall et al. 2022; Vela X-1, Forsblom et al. 2023; GRO J1008−57, Tsygankov et al. 2023; EXO 2030+375, Malacaria et al. 2023;

[⋆] Deceased.

X Persei, Mushtukov et al. 2023; LS V +44 17, Doroshenko V. et al., in prep.). In most cases, the observations revealed a rather low pulse-phase-averaged polarization degree (PD). The reason for the low PD is not completely clear. A toy model considering an upper layer of the NS atmosphere overheated by accretion has been proposed (Doroshenko et al. 2022). According to this model, the escaping radiation can be depolarized due to partial mode conversion when passing through the vacuum resonance region situated at the sharp temperature gradient between the cool, inner atmospheric layers and the upper, overheated layers. Also variations of the polarization angle (PA) with the pulsar phase lead to strong depolarization in the total signal.

The accreting X-ray pulsar GX 301−2 (also associated with 4U 1223−62) is one of *IXPE*'s targets. It is a high-mass X-ray binary system containing a slowly rotating ($P_{spin} \sim 680$ s, White et al. 1976) NS orbiting the hyper-giant donor star, Wray 977 (Hammerschlag-Hensberge et al. 1976). The donor star is a very massive (39–53 $M_\odot$) and large ($\sim 62\ R_\odot$), with a huge mass-loss rate of $\dot{M} \sim 10^{-5} M_\odot\,\mathrm{yr}^{-1}$ via a dense and slow (~ 300–$400\ \mathrm{km\,s}^{-1}$) wind (Kaper et al. 2006). The system inclination has been constrained to be in the range $52°$–$78°$, with an indication of a preference for an inclination closer to the lower end of the range (Leahy & Kostka 2008). A distance to the system of $3.53^{+0.40}_{-0.52}$ kpc was measured by Gaia (Treuz et al. 2018; Bailer-Jones et al. 2018). An orbital period of the system is known with a high accuracy, $P_{orb}=41.482\pm 0.001$ d (Doroshenko et al. 2010). The NS orbit is elliptic, with an eccentricity $e \sim 0.46$ (Koh et al. 1997), and the X-ray luminosity of the pulsar increases near the periastron, reaching $\sim 10^{37}\,\mathrm{erg\ s}^{-1}$(see Fig. 1 for the long-term light curve). The wind accretion picture in this system is very complicated. The outburst maximum is about 1.4 d before the periastron, and there is a secondary X-ray flux increase near the apoastron at the orbital phase 0.5 (Pravdo et al. 1995; Koh et al. 1997). It was even hypothesized that the NS in the system exhibits retrograde rotation (Mönkkönen et al. 2020).

The X-ray spectrum of the system was investigated by many observatories, including *NuSTAR* (see Nabizadeh et al. 2019, and references therein). The continuum X-ray spectrum is usual for an accreting XRP and is well described by a power-law model with a Fermi-Dirac cutoff (Fürst et al. 2018), with some additional components. These include two cyclotron resonant scattering features near 35 and 50 keV (Fürst et al. 2018), whose energies are positively correlated with the source X-ray luminosity, including variations over the pulse period (Fürst et al. 2018; Nabizadeh et al. 2019). It is necessary to mention a strong local absorption, which is also correlated with the observed luminosity. It can be as high as $(5 - 20) \times 10^{23}\ \mathrm{cm}^{-2}$ (see, e.g. Fürst et al. 2018; Nabizadeh et al. 2019; Doroshenko et al. 2010; Ji et al. 2021). Important components of the softer part of the X-ray spectrum are the iron Kα and Kβ lines, arising due to a reprocessing of X-rays in the matter surrounding the NS (see detailed analysis in Ji et al. 2021). Their strength is also strongly correlated with the source luminosity.

The first attempt to measure X-ray polarization of GX 301−2 was performed with balloon-borne hard X-ray polarimeter X-Calibur in the 15–35 keV energy band resulting in a non-detection (Abarr et al. 2020). Here we present the result of *IXPE* observations of GX 301−2. *IXPE* observations were accompanied by the simultaneous observations performed with the Mikhail Pavlinsky ART-XC telescope on the board of the *SRG* observatory. Archival observations of GX 301−2 performed by *NuSTAR* observatory were also used for the comparative analysis.
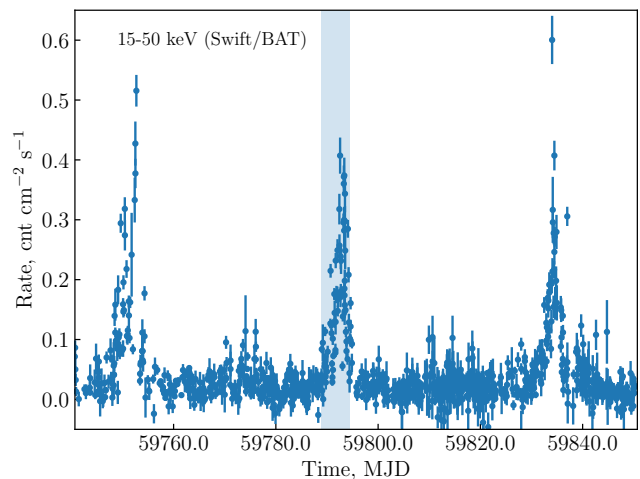
Fig. 1. The long-term light curve of GX 301−2 in the 15–50 keV energy band obtained with the *Swift*/BAT monitor. Shaded region represents the time of the *IXPE* observation.
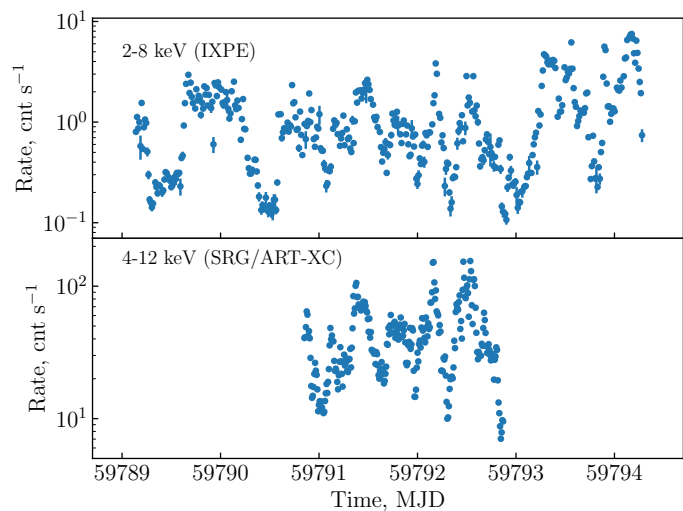

Fig. 2. Background subtracted light curve of the source in the 2–8 keV energy band observed with *IXPE* (top) and in the 4–12 keV band observed with *SRG*/ART-XC (bottom). Data from the three *IXPE* and seven ART-XC telescopes were combined.

2. Observations

The *IXPE* observatory, a NASA mission in partnership with the Italian space agency (see a detailed description in Weisskopf et al. 2022), was launched by a Falcon 9 rocket on 2021 December 9. There are three grazing incidence telescopes onboard the observatory. Each telescope comprises an X-ray mirror assembly and a polarization-sensitive detector unit (DU) equipped with a gas-pixel detector (GPD, Soffitta et al. 2021; Baldini et al. 2021). These instruments provide imaging polarimetry in the 2–8 keV energy band with a time resolution better than $10\,\mu$s.

IXPE observed GX 301−2 between 2022 July 29 and August 3 with a total exposure of $\simeq 290$ ks per telescope. The data have been processed with the ixpeobssim package version 30.2.1 (Baldini et al. 2022) using the CalDB released on 2022 November 17. Before the scientific analysis, a position offset correction and energy calibration were applied. Source photons were collected in a circular region with a radius $R_{src} = 70''$ centered at the GX 301−2 position. Background was extracted from an annulus

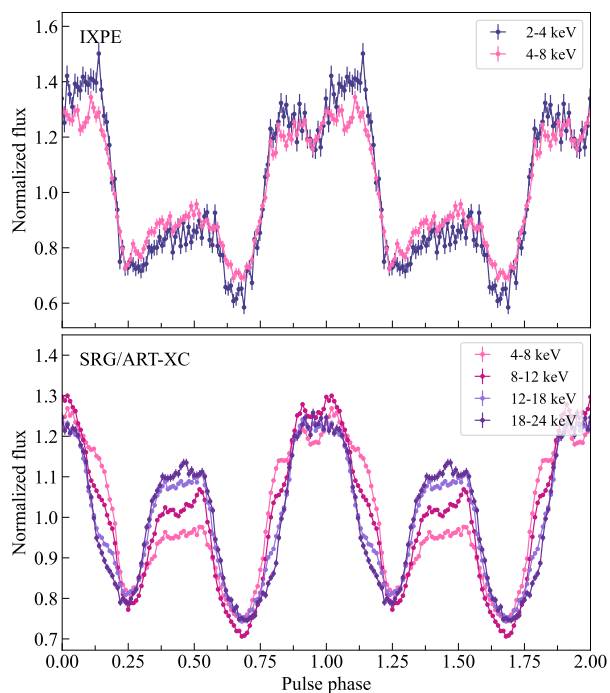**Fig. 3.** Pulse profiles of GX 301−2 obtained by *IXPE* and ART-XC in different energy bands.
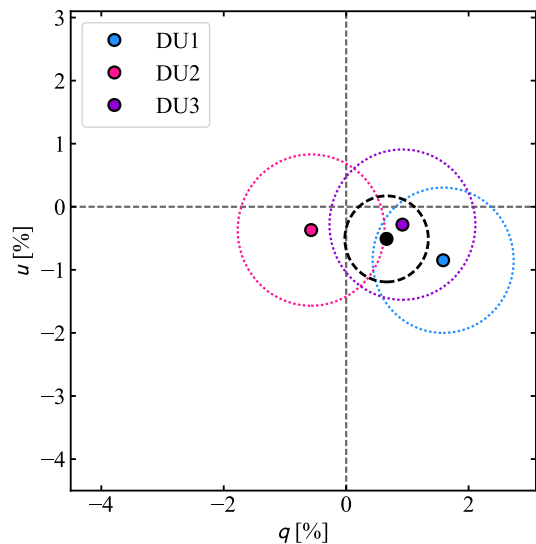

Fig. 4. Phase-averaged normalized Stokes parameters q and u for each DU, and combining the DUs (in black), for the full 2–8 keV energy band. The circle size corresponds to the uncertainty at 68% confidence level.

3. Results

3.1. Light curve and pulse profile

GX 301−2 was observed during a pre-periastron flare (at the orbital phase approximately 0.95–1.00) between 2022 July 29 and August 3, as seen in the light curve shown in Fig. 1 obtained by the *Swift*/BAT (Gehrels et al. 2004) monitor.[1] The light curves of GX 301−2 in the 2–8 energy band obtained with the *IXPE* observatory, as well as with *SRG*/ART-XC in the 4–12 keV band, are shown in Fig. 2. The spin period for GX 301−2 was measured to be P_{spin}=670.644(2) s. The pulsed fraction in the 2–8 keV energy range of *IXPE*, defined according to the equation $PF = (F_{\max} - F_{\min})/(F_{\max} + F_{\min})$, where $F_{\max}$ and $F_{\min}$ are the maximum and minimum count rates in the pulse profile, respectively, was determined to be $PF = 34.0\% \pm 1.1\%$. The pulse profiles of GX 301−2 as seen by *IXPE* and ART-XC in different energy bands are shown in Fig. 3. Phase-zero was chosen to coincide for the *IXPE* and ART-XC observations, and the phase-shift was determined from comparing the pulse profiles in the 4–8 keV energy band for both observations.

3.2. Polarimetric analysis

The polarimetric properties of GX 301−2 were first analyzed utilizing the `pcube` algorithm (`xpbin` tool) in the IXPEOBSSIM package, which has been implemented following the formalism by Kislat et al. (2015). For the subsequent analysis, the unweighted approach (i.e. all events are given the same weight) has been used, and as a result of the high source count rate, background subtraction was not applied (Di Marco et al. 2023). The normalized Stokes parameters $q = Q/I$ and $u = U/I$ for the full 2–8 keV energy range of *IXPE* are shown in Fig. 4. We see that no significant polarization is detected. The data were subsequently divided into 6 energy bins to study a possible energy dependence of the polarization properties for GX 301−2. The measured Stokes parameters are consistent with zero within 2σ.

with the inner and outer radii of $2R_{\mathrm{src}}$ and $4R_{\mathrm{src}}$, respectively. In the 2–8 keV band, the background makes up about 1.2% of the total count rate in the source region. The event arrival times were corrected to the Solar system barycenter using the standard `barycorr` tool from the FTOOLS package and accounting for the effects of binary motion using the orbital parameters from Doroshenko et al. (2010).

The flux (Stokes parameter I) energy spectra have been binned to have at least 30 counts per energy channel. The same energy binning was also applied to the spectra of the Stokes parameters Q and U. Because of the high source count rate and the low background level, the background was not subtracted as recommended by Di Marco et al. (2023). The unweighted analysis (i.e. all events are taken into account independently of the quality of track reconstruction) of the *IXPE* data has been applied. All the spectra were fitted with the XSPEC package (Arnaud 1996) using the instrument response functions of version 12 and a χ^2 statistic. The uncertainties are given at the 68.3% confidence level unless stated otherwise.

The Mikhail Pavlinsky ART-XC telescope (Pavlinsky et al. 2021) is a grazing incidence focusing X-ray telescope on board the *SRG* observatory (Sunyaev et al. 2021) which provides imaging, timing and spectroscopy in the 4–30 keV energy range. The telescope consists of seven identical modules with the total effective area of ~450 cm^2 at 8 keV, angular resolution of 45″ energy resolution of 1.4 keV at 6 keV and timing resolution of 23 μs. The ART-XC telescope carried out simultaneous observations of GX 301−2 with *IXPE* starting on 2022 July 30, 20:25 and ending on August 1, 20:50 (UTC) with the total exposure of ~160 ks. ART-XC data were processed with the analysis software ARTPRODUCTS v1.0 with the CALDB version 20220908.

Table 1. Spectropolarimetric parameters in different pulse-phase bins.

Phase	q (%)	u (%)	N_H (10^{22} cm^{-2})	Photon index	PD (%)	PA (deg)	χ^2/d.o.f.
0.000–0.058	-10.6 ± 3.2	-0.5 ± 3.2	24.4 ± 1.2	0.15 ± 0.14	9.9 ± 3.2	89 ± 9	990.5/1017
0.058–0.193	0.1 ± 2.0	1.0 ± 2.0	23.4 ± 0.7	-0.08 ± 0.08	$1.9^{+1.9}_{-1.9}$ (< 6.8)	80 ± 30	1262.3/1245
0.193–0.328	-0.9 ± 2.0	0.9 ± 2.0	25.1 ± 0.7	0.11 ± 0.08	$2.0^{+1.9}_{-1.9}$ (< 6.8)	66 ± 34	1342.5/1236
0.328–0.463	4.1 ± 2.1	2.5 ± 2.1	24.3 ± 0.7	0.12 ± 0.09	4.9 ± 2.1	15 ± 13	1253.7/1212
0.463–0.603	1.5 ± 1.8	0.0 ± 1.8	26.3 ± 0.6	0.45 ± 0.07	$0.2^{+1.7}_{-0.2}$ (< 4.6)	82 ± 90	1320.5/1269
0.603–0.733	3.8 ± 1.7	-0.9 ± 1.7	25.6 ± 0.6	0.30 ± 0.06	4.3 ± 1.6	-14 ± 11	1397.8/1278
0.733–0.813	0.9 ± 2.2	-8.0 ± 2.2	24.8 ± 0.7	0.24 ± 0.08	7.7 ± 2.0	-46 ± 7	1270.5/1206
0.813–0.893	0.6 ± 2.1	-1.2 ± 2.1	26.5 ± 0.7	0.59 ± 0.08	2.8 ± 1.9	-13 ± 22	1272.8/1212
0.893–1.000	-1.5 ± 2.0	0.9 ± 2.0	26.8 ± 0.7	0.59 ± 0.08	$1.6^{+1.9}_{-1.6}$ (< 6.5)	72 ± 40	1241.4/1227

Notes. Normalized Stokes q and u parameters are obtained from the `pcube` algorithm. The spectral parameters as well as PD and PA are obtained by the spectro-polarimetric analysis with xspec. The uncertainties are given at the 68.3% (1σ) confidence level. The uncertainties on PD and PA are computed using `error` command in xspec with $\Delta\chi^2 = 1$ for one parameter of interest. The upper limits to the PD (in parentheses) correspond to the 99% confidence level ($\Delta\chi^2 = 6.635$) and are quoted when the PD is consistent with zero within 1σ.
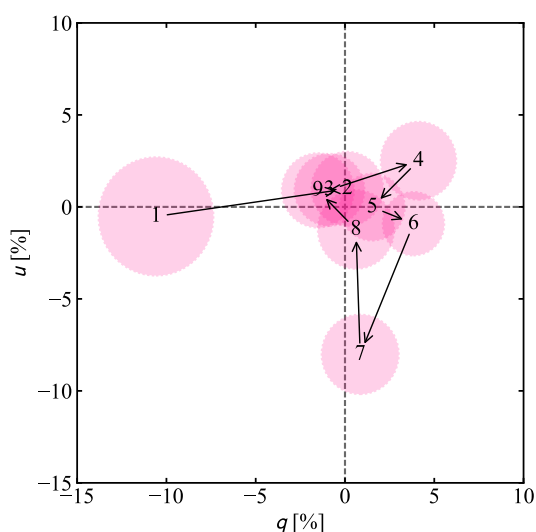

Fig. 5. Normalized Stokes parameters q and u for the phase-resolved polarimetric analysis using `pcube` (DUs combined), for the full 2–8 keV energy band. Each circle corresponds to a separate phase bin and is numbered according to its order as referenced in Table 1. The radius of the circle corresponds to a 1σ uncertainty.

Table 2. Spectral parameters for the best-fit model obtained from the phase-averaged spectro-polarimetric analysis with xspec.

Parameter	Value	Unit
N_H	24.6 ± 0.4	10^{22} cm^{-2}
E_{Fe}	6.35 ± 0.01	keV
σ_{Fe}	0.27 ± 0.03	keV
const$_{DU2}$	0.960 ± 0.007	
const$_{DU3}$	0.927 ± 0.007	
hoton index	0.29 ± 0.05	
PD	0.67 ± 0.64 (< 2.3)	%
PA	-36 ± 27	deg
Flux$_{2-8\ keV}$	$8.58^{+0.03}_{-0.08}$	10^{-10} erg cm^{-2} s^{-1}
Luminosity$_{2-8\ keV}$	1.3×10^{36}	erg s^{-1} at $d = 3.5$ kpc
χ^2 (d.o.f.)	1373.67 (1322)	

Notes. The uncertainties are given at the 68.3% (1σ) confidence level and obtained using `error` command in xspec with $\Delta\chi^2 = 1$ for one parameter of interest. The upper limit to the PD (in parenthesis) correspond to the 99% confidence level ($\Delta\chi^2 = 6.635$).

The polarization properties of XRPs are expected to be strongly variable with pulse phase, and therefore next, we performed a phase-resolved polarimetric analysis using the `pcube`-algorithm. The data were divided into nine separate phase bins in the full 2–8 keV range. The results are displayed in Figs. 5 and 6 and are given in Table 1.

The full spectro-polarimetric analysis was performed with the following steps. The Stokes spectra I, Q, and U for the source region were extracted using the `xpbin` tool's PHA1, PHA1Q, and PHA1U algorithms in ixpeobssim, resulting in a data set consisting of nine spectra (three for each DU). The xspec package (version 12.12.1) (Arnaud 1996), which is a part of the standard high-energy astrophysics software suite HEASOFT, was used for the spectro-polarimetric analysis studying the polarization properties as a function of energy.

The continuum spectra of XRPs are typically described by purely phenomenological spectral models, such as a power law with a cut-off at high energies. Several models of varying complexity have been used to describe the spectral continuum of

GX 301−2. However, for the energy resolution and energy range of *IXPE*, a more simplified model was used to fit the spectra. This spectral model consists of an absorbed power law (for the absorption we used `tbabs` model with the abundances from Wilms et al. 2000). Additionally, a prominent iron emission line (complex) is also observed, and therefore a Gaussian component was introduced. A re-normalization constant was used to account for possible discrepancies between the separate DUs (`const`), and for DU1 it was fixed at unity. Finally, the `polconst` polarization model, assuming a constant PD and PA with energy, was applied to the power law, while the Gaussian component was assumed to be unpolarized. The resulting model

`tbabs×(polconst×powerlaw+gaussian)×const`

was used to fit both the phase-averaged and the phase-resolved data. A systematic error of 5% was added over the entire 2–8 keV energy range for the phase-averaged spectro-polarimetric analysis. The results of the spectral fitting of the phase-averaged data are given in Table 2. For the phase-averaged data, we do not detect any significant polarization, with a 99% upper limit of PD< 2.3%. The `polconst` polarization model was replaced with the `pollin` (linear energy dependence of the PD and PA) and `polpow` (power-law energy dependence of the PD and PA)
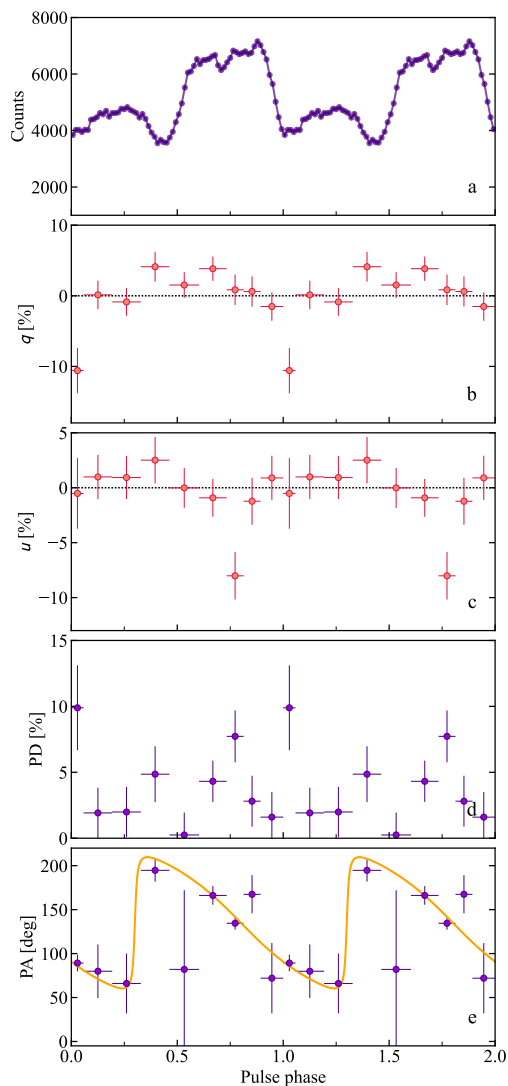
Fig. 6. Results from the pulse-phase-resolved analysis of GX 301−2 in the 2–8 keV range, combining data from all DUs. *Panel (a)*: Pulse profile. *Panels (b)* and *(c)*: Dependence of the Stokes q and u parameters obtained from the pcube algorithm on the pulse phase. *Panels (d)* and *(e)*: PD and PA obtained from the phase-resolved spectro-polarimetric analysis using xspec. The orange curve in panel (e) shows the best-fit RVM with $i_p = 135°$, $\theta = 43°$, $\chi_p = 135°$, and $\phi_0/(2\pi) = -0.2$ to the PAs obtained from the pairs of (q, u) (see Sect. 4.1).

models, however, neither one gave an improvement of the fit, therefore we find no evidence for an energy-dependent polarization.

The same model used for the phase-averaged spectro-polarimetric analysis, was used to fit the phase-resolved spectra, however, the cross-calibration constants for DU2 and DU3 were fixed to the best-fit values obtained for the phase-averaged analysis (see Table 2). Due to low statistics in the phase-resolved spectra, the energy and width of the Gaussian component were fixed at the best-fit values from Table 2. The steppar command in xspec was used to obtain the constraints on polarization parameters. The resulting PD and PA are shown in Fig. 6d,e and given in Table 1. The two different approaches using pcube and xspec give compatible results. The 2D contour plots at 68.3%, 95.45% and 99.73% confidence levels for the PD and PA pair are presented in Fig. 7.

4. Discussion

4.1. Pulsar geometry

The rotating-vector model (RVM, Radhakrishnan & Cooke 1969; Poutanen 2020) can be used to constrain the pulsar geometry. In this model the PA is given by

$$\tan(PA - \chi_p) = \frac{-\sin\theta \, \sin(\phi - \phi_0)}{\sin i_p \cos\theta - \cos i_p \sin\theta \cos(\phi - \phi_0)}, \quad (1)$$

where χ_p is the position angle (measured from north to east) of the pulsar angular momentum, i_p is the inclination of the pulsar spin to the line of sight, θ is the angle between the magnetic dipole and the spin axis, and ϕ_0 is the phase when the northern magnetic pole passes in front of the observer.

In spite of the fact that the observed PAs are not well determined in many phase bins, we can use measurements of the Stokes q and u parameters (which are normally distributed) in all phase bins to get constraints on RVM parameters. For any (q, u) and their error σ_p, the probability density function of the PA, ψ, can be computed as (Naghizadeh-Khouei & Clarke 1993):

$$G(\psi) = \frac{1}{\sqrt{\pi}} \left\{ \frac{1}{\sqrt{\pi}} + \eta e^{\eta^2} \left[1 + \mathrm{erf}(\eta) \right] \right\} e^{-p_0^2/2}. \quad (2)$$

Here $p_0 = \sqrt{q^2 + u^2}/\sigma_p$ is the 'measured' PD in units of the error, $\eta = p_0 \cos[2(\psi - \psi_0)]/\sqrt{2}$, $\psi_0 = \frac{1}{2}\arctan(u/q)$ is the central PA obtained from the Stokes parameters, and erf is the error function.

We fit the RVM to the pulse-phase dependence of the (q, u) obtained from pcube using the affine invariant Markov chain Monte Carlo ensemble sampler EMCEE package of PYTHON (Foreman-Mackey et al. 2013) and applying the likelihood function $L = \Pi_i G(\psi_i)$ with the product taken over all phase bins. The covariance plot for the RVM parameters is shown Fig. 8. We note that fitting the PA values obtained from xspec with the RVM assuming Gaussian errors and χ^2 statistics gives nearly identical results.

We see that the inclination and the magnetic obliquity are rather well determined: $i_p = 135° \pm 17°$ and $\theta = 43° \pm 12°$. On the other hand, other parameters allow multiple solutions. The reason for that is simple: most of the detections of polarization are marginal only. The posterior distribution of χ_p has three broad peaks at 25°, 80°, and the strongest one at 135°. These peaks correspond to the peaks in $\phi_0/(2\pi)$ at 0.4, 0.0, and −0.2, respectively.

As a test of our RVM fit to the phase-binned data, we now apply an alternative unbinned photon-by-photon analysis (González-Caniulef et al. 2023). We run MCMC simulations to get the estimates on the RVM parameters. The results are shown in Fig. 9. The photoelectron emission angles for each event are used to constrain a RVM that predicts the distribution of photoelectron angles as a function of the phase. The PA of the best-fit RVM is depicted by an orange curve in Fig. 10. Furthermore, for illustration we obtained a maximum likelihood estimate of the PD and PA assuming constant polarization in each of fourteen phase bins as shown by the error bars in the lower two panels of Fig. 10. The mean PD in the frame of the magnetic pole is about 2.5%. The best-fit $i_p = 129° \pm 16°$ and $\theta = 47° \pm 12°$ are in perfect agreement with the RVM fit to the phase-binned data. The position angle of the pulsar spin and the zero phase ϕ_0, are also not well determined. Here too, the posterior distributions show multiple peaks and strong correlation between these parameters. We see three peaks in χ_p and ϕ_0 at positions close to those of the phase-binned RVM fits.
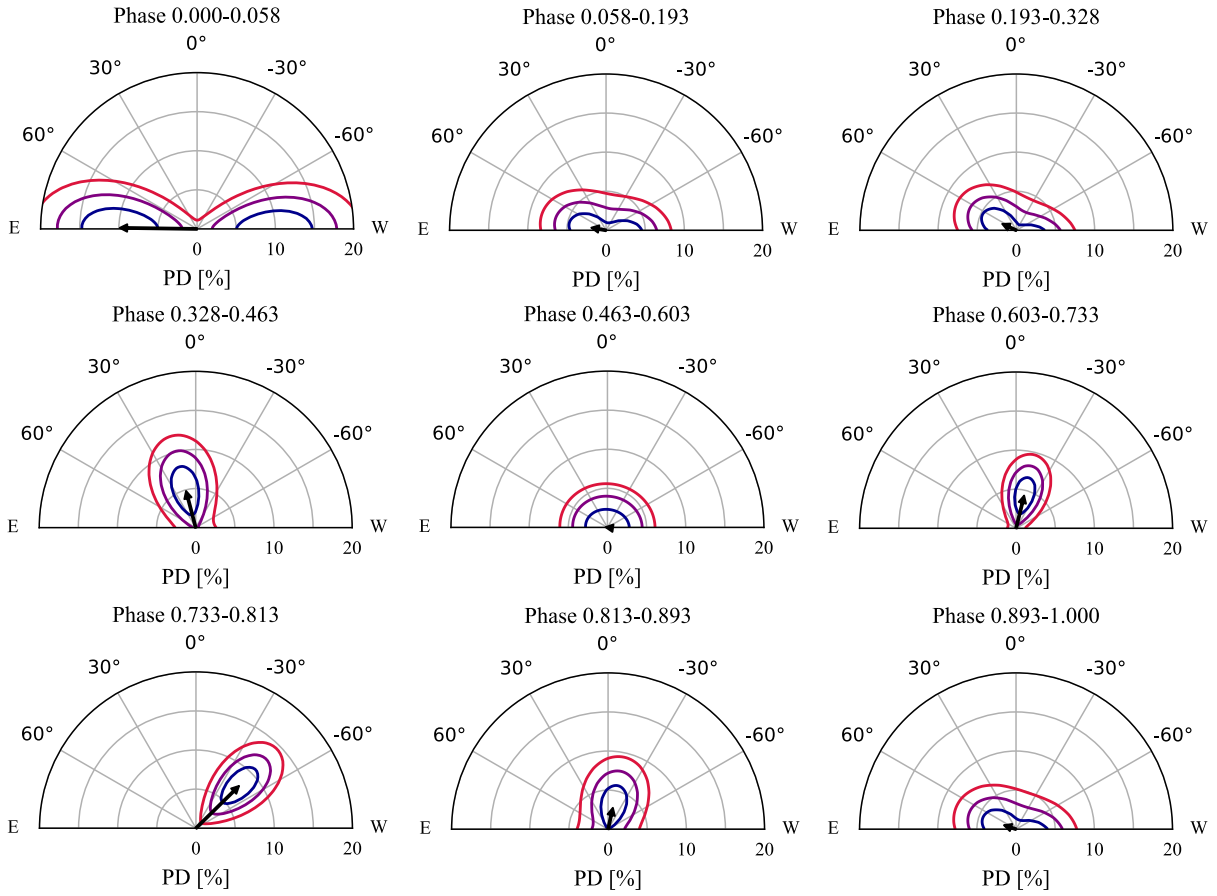
Fig. 7. Polarization vectors of GX 301−2 from the results of the phase-resolved spectro-polarimetric analysis. Contours at 68.3, 95.45 and 99.73% confidence levels, are shown in blue, purple, and red, respectively.
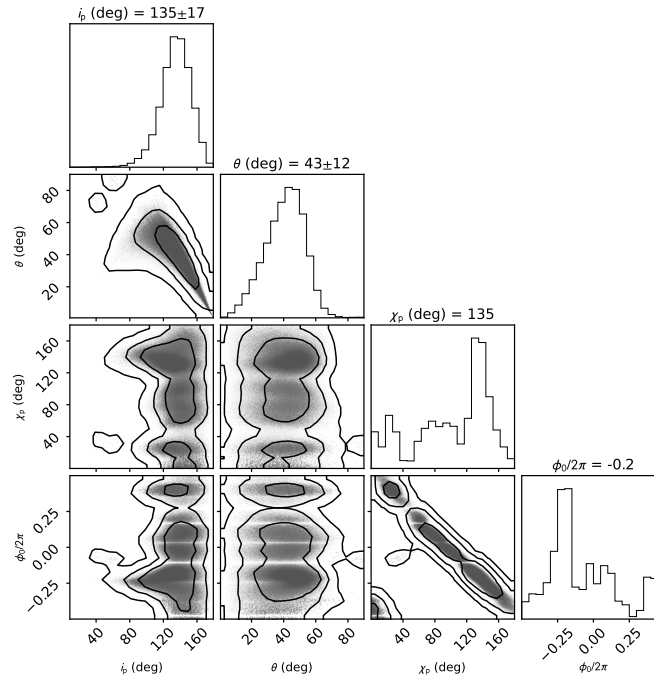

Fig. 8. Corner plot of the posterior distribution for parameters of the RVM model fitted directly to the (q, u) values using likelihood function (2). The two-dimensional contours correspond to 68.3%, 95.45% and 99.73% confidence levels. The histograms show the normalized one-dimensional distributions for a given parameter derived from the posterior samples.
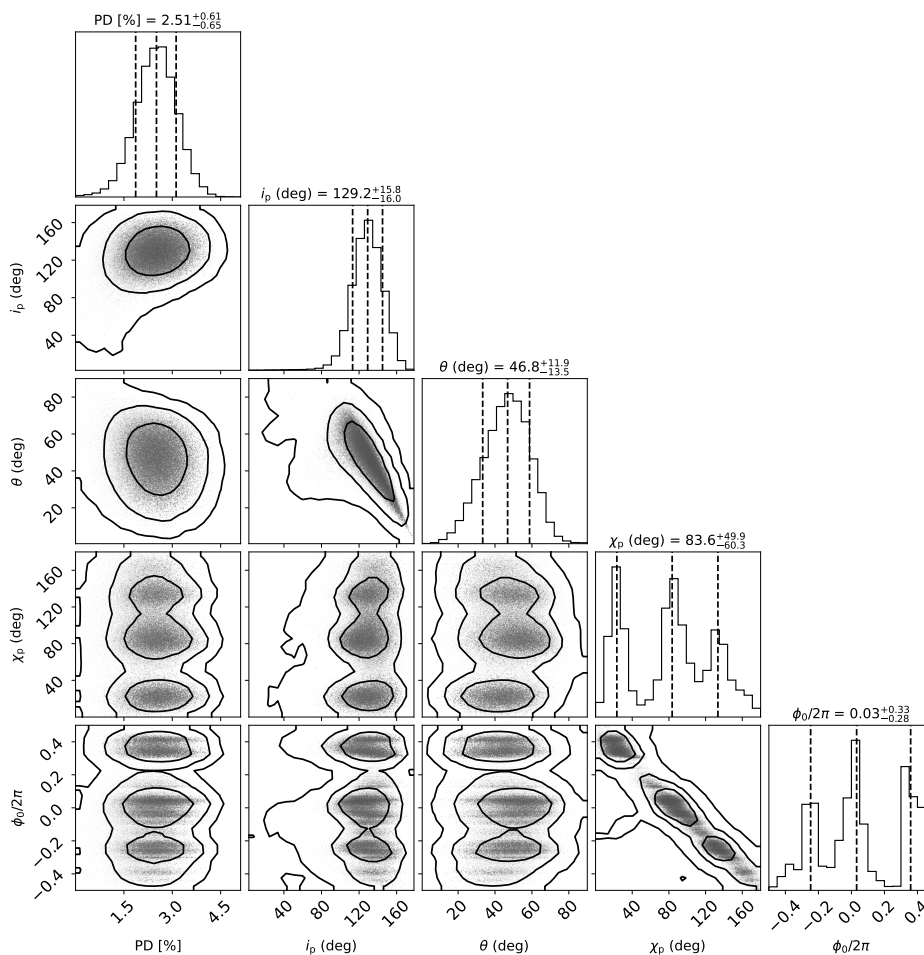
Fig. 9. Same as Fig. 8 but obtained via unbinned analysis (González-Caniulef et al. 2023).

4.2. Scattering by the stellar wind

The relatively low PD detected for GX 301−2 is in line with other XRPs observed with *IXPE* (Cen X-3, Her X-1, GRO J1008−57, Vela X-1, 4U 1626−67, EXO 2030+375). The low PD is in contradiction with previous theoretical predictions, which estimate PDs as high as 80% (Meszaros et al. 1988; Caiazzo & Heyl 2021). It is interesting, that more luminous XRPs ($L_X \geq 10^{37}$ erg s^{-1}) demonstrate significantly higher phase-averaged polarization degree, up to 6%–10% in Her X-1 (Doroshenko et al. 2022) and 4%–6% in Cen X-3 (Tsygankov et al. 2022) than the less luminous XRPs. It can be connected with difference in the physical structure of the radiation regions. In particular, Doroshenko et al. (2022) proposed a model to explain the low PD by means of an overheated upper NS atmosphere, with a sharp temperature gradient between the overheated upper atmospheric layer and the underlying cooler layer. The most important component of this model is the point of the so called vacuum resonance, where the mode conversion occurs. If the point of vacuum resonance is located at the transition between the hot and cool layer, this may result in the low PD. The described model can be correct for relatively low local accretion rates only. In addition to an intrinsic low polarization, we considered possibilities that the X-ray radiation can be depolarized in the plasma surrounding the X-ray pulsar, because GX 301−2 is significantly more obscured than other XRPs. A detailed qualitative analysis of the depolarization reasons was presented in

Tsygankov et al. (2022). Here we consider depolarization of X-ray flux passing through the surrounding plasma in more detail.

GX 301−2 is subject to the dense stellar wind of its massive companion star. This wind is characterized by a relatively slow velocity, but a huge mass-loss rate. Scattering in the wind is expected to reduce the intrinsic polarization. Whether or not the wind is able to affect the observed polarization will depend on the wind Thomson optical depth, which can be estimated as (Kallman et al. 2015) $\tau_T \simeq 2 \times 10^{-4} \dot{M}_8 a_{12}^{-1} v_{x8}^{-1}$, where $\dot{M}_8$ is the mass loss rate in units $10^{-8} M_\odot$ yr^{-1}), a_{12} is the separation in units 10^{12} cm, and v_{x8} is the wind velocity at the X-ray source in units 1000 km s^{-1}. For GX 301−2, taking typical values for the wind parameters $\dot{M}_8 \sim 10^3$ and $v_{x8} = 0.3$, as well as the orbital separation at periastron passage $a = a_p \sim 95 R_\odot$ (i.e. $a_{12} = 6.7$), we get the optical depth through the wind of $\tau_T \sim 0.1$.

The estimate presented above was made under the assumption of a homogeneous spherically symmetric wind. However, the orbiting NS disturbs the stellar wind leading to various inhomogeneities in the vicinity of the XRP. As a result, the optical depth along the line of sight can be larger. In the first approximation, this optical depth can be estimated from N_H assuming that the number of electrons along the line of sight is the same. For the N_H in the range $(5 - 20) \times 10^{23}$ cm^{-2} (Fürst et al. 2018; Nabizadeh et al. 2019; Doroshenko et al. 2010; Ji et al. 2021), we get $\tau_T \approx \sigma_T N_H \approx 0.3$–1.2.

We now consider how the polarized radiation will be depolarized when it is transmitted through the ionized plasma slab.
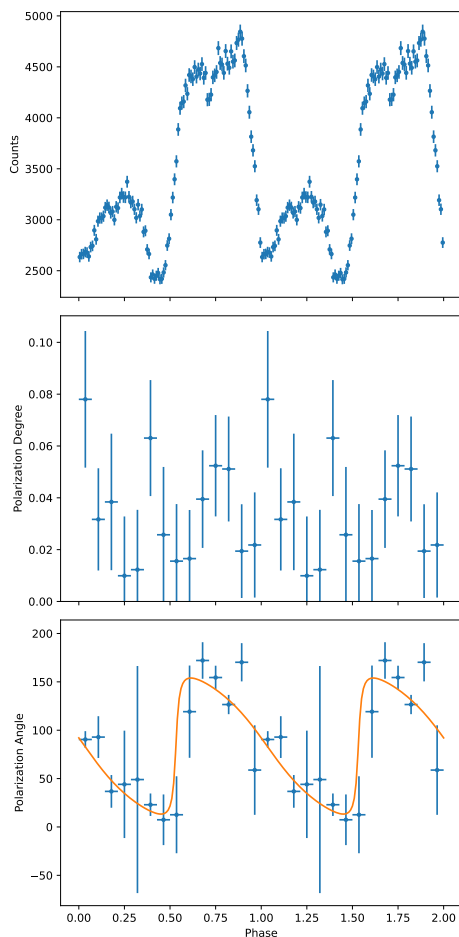
Fig. 10. Pulse profile, PD, and PA obtained from the maximum-likelihood analysis (González-Caniulef et al. 2023). The error bars give the most likely values of PD and PA with $\Delta \ln L = 0.5$ (1σ) confidence regions. The orange curve at the bottom panel shows the best-fit RVM solution with the following parameters $i_p = 129°$, $\theta = 47°$, $\chi_p = 84°$, $\phi_0/(2\pi) = 0.03$.

We solved the radiation transfer equation in two polarization modes (see details in Suleimanov et al. 2023). We neglected emission by the plasma itself and assumed that the slab is situated far enough from the X-ray source, so that the external flux is directed normally to the slab surface. We define the depolarization factor dPD=PD′/PD as the ratio of the PD of the transmitted radiation to that of the incident one. The dependence of dPD on the slab optical depth τ is well approximated by the expression:

$$\text{dPD} = A \left[\exp\left(\frac{\tau - \tau_*}{\Delta\tau} \right) + 1 \right]^{-1}, \qquad (3)$$

where $\tau_* = 4.6$ is the optical depth providing dPD=0.5, $\Delta\tau = 1.2$ is a smearing parameter, and $A = \exp\left(-\tau_*/\Delta\tau \right) + 1 \approx 1.02$ is a normalization constant. We note that τ is the total optical depth including not only electron scattering, but free-free and bound-free absorption as well. We see that in principle the PD can decrease by a factor of two for $\tau \sim 5$, but such a large optical depth of the envelope around the XRP is clearly too large and would lead to a dramatic decrease of the pulsed fraction which is not observed. We conclude here that scattering in the wind is not a likely source of a relatively low PD.

In addition to scattering, the wind also may reprocess some radiation of the XRP. In particular, the strength of fluorescent

iron lines Kα and Kβ observed from GX 301−2 (see, e.g., Ji et al. 2021) correlates with the X-ray flux and with the local absorption. The lines contribute about 10% of the flux in the *IXPE* band. Thus, these unpolarized lines can produce a depolarization factor of about 0.9, which means that they cannot significantly depolarize the XRP radiation.

5. Summary

GX 301−2 was observed by *IXPE* between 2022 July 29 and August 3, during a pre-periastron flare. Simultaneous observations of GX 301−2 were carried out by the ART-XC telescope between 2022 July 30 and August 1. The main results of our study of the polarimetric properties of GX 301−2 can be summarized as follows:

1. We have not detected a significant polarization in the phase-averaged data, with an upper limit to the PD of 2.3% (at 99% confidence level) in the full 2–8 keV energy range of *IXPE*. Likewise, significant polarization was not detected in any energy bin in the phase-averaged data.

2. The phase-resolved polarimetric analysis revealed a significant detection of polarization in two out of nine phase bins and marginal detection in three bins, with the PD ranging from ∼3% to ∼10%, and the PA varying in a very wide range from ∼0° to ∼160°.

3. Application of the RVM to the phase-resolved PA (accounting even for the points with low significance) allowed us to estimate the inclination of the NS rotation axis to the line of sight of $i_p \approx 130° − 140°$ and the magnetic obliquity of $\theta \approx 40° − 50°$. The measured pulsar spin inclination is in good agreement with the orbital inclination of 52°–78° with some preference towards lower values determined by Leahy & Kostka (2008). We note that the preferred lowest orbital inclination is equivalent to 128°. On the other hand, the NS in the system might rotate retrogradely as was proposed by Mönkkönen et al. (2020). The position angle of the pulsar spin and the zero phase, when the northern magnetic pole passes in front of the observer, allow multiple solutions. We find excellent agreement between phase-binned and unbinned analysis.

4. The contribution of the reprocessed radiation and scattering in the surrounding matter can depolarize the intrinsic XRP flux by no more than 10%–15%.

References

Abarr, Q., Baring, M., Beheshtipour, B., et al. 2020, ApJ, 891, 70

Arnaud, K. A. 1996, in ASP Conf. Ser., Vol. 101, Astronomical Data Analysis Software and Systems V, ed. G. H. Jacoby & J. Barnes (San Francisco: Astron. Soc. Pac.), 17–20

Bailer-Jones, C. A. L., Rybizki, J., Fouesneau, M., Mantelet, G., & Andrae, R. 2018, AJ, 156, 58

Baldini, L., Barbanera, M., Bellazzini, R., et al. 2021, Astroparticle Physics, 133, 102628

Baldini, L., Bucciantini, N., Lalla, N. D., et al. 2022, SoftwareX, 19, 101194

Basko, M. M. & Sunyaev, R. A. 1976, MNRAS, 175, 395

Becker, P. A., Klochkov, D., Schönherr, G., et al. 2012, A&A, 544, A123

Caiazzo, I. & Heyl, J. 2021, MNRAS, 501, 109

Di Marco, A., Soffitta, P., Costa, E., et al. 2023, AJ, 165, 143

Doroshenko, V., Poutanen, J., Tsygankov, S. S., et al. 2022, Nature Astronomy, 6, 1433

Doroshenko, V., Santangelo, A., Suleimanov, V., et al. 2010, A&A, 515, A10

Foreman-Mackey, D., Hogg, D. W., Lang, D., & Goodman, J. 2013, PASP, 125, 306

Forsblom, S. V., Poutanen, J., Tsygankov, S. S., et al. 2023, ApJ, 947, L20

Fürst, F., Falkner, S., Marcu-Cheatham, D., et al. 2018, A&A, 620, A153

Gehrels, N., Chincarini, G., Giommi, P., et al. 2004, ApJ, 611, 1005

González-Caniulef, D., Caiazzo, I., & Heyl, J. 2023, MNRAS, 519, 5902

Hammerschlag-Hensberge, G., Zuiderwijk, E. J., van den Heuvel, E. P. J., & Hensberge, H. 1976, A&A, 49, 321

Harding, A. K. & Lai, D. 2006, Reports on Progress in Physics, 69, 2631

Ji, L., Doroshenko, V., Suleimanov, V., et al. 2021, MNRAS, 501, 2522

Kallman, T., Dorodnitsyn, A., & Blondin, J. 2015, ApJ, 815, 53

Kaper, L., van der Meer, A., & Najarro, F. 2006, A&A, 457, 595

Kislat, F., Clark, B., Beilicke, M., & Krawczynski, H. 2015, Astroparticle Physics, 68, 45

Koh, D. T., Bildsten, L., Chakrabarty, D., et al. 1997, ApJ, 479, 933

Leahy, D. A. & Kostka, M. 2008, MNRAS, 384, 747

Malacaria, C., Heyl, J., Doroshenko, V., et al. 2023, A&A, in press, arXiv:2304.00925

Marshall, H. L., Ng, M., Rogantini, D., et al. 2022, ApJ, 940, 70

Meszaros, P., Novick, R., Szentgyorgyi, A., Chanan, G. A., & Weisskopf, M. C. 1988, ApJ, 324, 1056

Mönkkönen, J., Doroshenko, V., Tsygankov, S. S., et al. 2020, MNRAS, 494, 2178

Mushtukov, A. & Tsygankov, S. 2022, in Handbook of X-ray and Gamma-ray Astrophysics, ed. C. Bambi & A. Santangelo (Singapore: Springer), arXiv:2204.14185

Mushtukov, A. A., Suleimanov, V. F., Tsygankov, S. S., & Poutanen, J. 2015, MNRAS, 447, 1847

Mushtukov, A. A., Tsygankov, S. S., Poutanen, J., et al. 2023, MNRAS, submitted, arXiv:2303.17325

Nabizadeh, A., Mönkkönen, J., Tsygankov, S. S., et al. 2019, A&A, 629, A101

Naghizadeh-Khouei, J. & Clarke, D. 1993, A&A, 274, 968

Pavlinsky, M., Tkachenko, A., Levin, V., et al. 2021, A&A, 650, A42

Poutanen, J. 2020, A&A, 641, A166

Pravdo, S. H., Day, C. S. R., Angelini, L., et al. 1995, ApJ, 454, 872

Radhakrishnan, V. & Cooke, D. J. 1969, Astrophys. Lett., 3, 225

Soffitta, P., Baldini, L., Bellazzini, R., et al. 2021, AJ, 162, 208

Suleimanov, V. F., Poutanen, J., Doroshenko, V., & Werner, K. 2023, A&A, 673, A15

Sunyaev, R., Arefiev, V., Babyshkin, V., et al. 2021, A&A, 656, A132

Treuz, S., Doroshenko, V., Santangelo, A., & Staubert, R. 2018, arXiv e-prints, arXiv:1806.11397

Tsygankov, S. S., Doroshenko, V., Mushtukov, A. A., et al. 2023, A&A, in press, arXiv:2302.06680

Tsygankov, S. S., Doroshenko, V., Poutanen, J., et al. 2022, ApJ, 941, L14

Weisskopf, M. C., Soffitta, P., Baldini, L., et al. 2022, JATIS, 8, 026002

White, N. E., Mason, K. O., Huckle, H. E., Charles, P. A., & Sanford, P. W. 1976, ApJ, 209, L119

Wilms, J., Allen, A., & McCray, R. 2000, ApJ, 542, 914

[1] Institut für Astronomie und Astrophysik, Universität Tübingen, Sand 1, D-72076 Tübingen, Germany
e-mail: suleimanov@astro.uni-tuebingen.de

[2] Department of Physics and Astronomy, FI-20014 University of Turku, Finland

[3] INAF Istituto di Astrofisica e Planetologia Spaziali, Via del Fosso del Cavaliere 100, 00133 Roma, Italy

[4] Institut de Recherche en Astrophysique et Planétologie, UPS-OMP, CNRS, CNES, 9 avenue du Colonel Roche, BP 44346 31028, Toulouse CEDEX 4, France

[5] University of British Columbia, Vancouver, BC V6T 1Z4, Canada

[6] Space Research Institute (IKI) of Russian Academy of Sciences, Prosoyuznaya ul 84/32, 117997 Moscow, Russian Federation

[7] International Space Science Institute, Hallerstrasse 6, 3012 Bern, Switzerland

[8] Astrophysics, Department of Physics, University of Oxford, Denys Wilkinson Building, Keble Road, Oxford OX1 3RH, UK

[9] National Research University Higher School of Economics, Faculty of Physics, 101000, Myasnitskaya ul. 20, Moscow, Russia

[10] Instituto de Astrofísicade Andalucía – CSIC, Glorieta de la Astronomía s/n, 18008 Granada, Spain

[11] INAF Osservatorio Astronomico di Roma, Via Frascati 33, 00040 Monte Porzio Catone (RM), Italy

[12] Space Science Data Center, Agenzia Spaziale Italiana, Via del Politecnico snc, 00133 Roma, Italy

[13] INAF Osservatorio Astronomico di Cagliari, Via della Scienza 5, 09047 Selargius (CA), Italy

[14] Istituto Nazionale di Fisica Nucleare, Sezione di Pisa, Largo B. Pontecorvo 3, 56127 Pisa, Italy

[15] Dipartimento di Fisica, Università di Pisa, Largo B. Pontecorvo 3, 56127 Pisa, Italy

[16] NASA Marshall Space Flight Center, Huntsville, AL 35812, USA

[17] Dipartimento di Matematica e Fisica, Università degli Studi Roma Tre, via della Vasca Navale 84, 00146 Roma, Italy

[18] Istituto Nazionale di Fisica Nucleare, Sezione di Torino, Via Pietro Giuria 1, 10125 Torino, Italy

[19] Dipartimento di Fisica, Università degli Studi di Torino, Via Pietro Giuria 1, 10125 Torino, Italy

[20] INAF Osservatorio Astrofisico di Arcetri, Largo Enrico Fermi 5, 50125 Firenze, Italy

[21] Dipartimento di Fisica e Astronomia, Università degli Studi di Firenze, Via Sansone 1, 50019 Sesto Fiorentino (FI), Italy

[22] Istituto Nazionale di Fisica Nucleare, Sezione di Firenze, Via Sansone 1, 50019 Sesto Fiorentino (FI), Italy

[23] Agenzia Spaziale Italiana, Via del Politecnico snc, 00133 Roma, Italy

[24] Science and Technology Institute, Universities Space Research Association, Huntsville, AL 35805, USA

[25] Istituto Nazionale di Fisica Nucleare, Sezione di Roma "Tor Vergata", Via della Ricerca Scientifica 1, 00133 Roma, Italy

[26] Department of Physics and Kavli Institute for Particle Astrophysics and Cosmology, Stanford University, Stanford, California 94305, USA

[27] Université Grenoble Alpes, CNRS, IPAG, 38000 Grenoble, France

[28] Astronomical Institute of the Czech Academy of Sciences, Boční II 1401/1, 14100 Praha 4, Czech Republic

[29] RIKEN Cluster for Pioneering Research, 2-1 Hirosawa, Wako, Saitama 351-0198, Japan

[30] Cahill Center for Astronomy and Astrophysics, California Institute of Technology, Pasadena, CA 91125, USA

[31] Yamagata University,1-4-12 Kojirakawa-machi, Yamagata-shi 990-8560, Japan

[32] Osaka University, 1-1 Yamadaoka, Suita, Osaka 565-0871, Japan

[33] International Center for Hadron Astrophysics, Chiba University, Chiba 263-8522, Japan

[34] Institute for Astrophysical Research, Boston University, 725 Commonwealth Avenue, Boston, MA 02215, USA

[35] Department of Astrophysics, St. Petersburg State University, Universitetsky pr. 28, Petrodvoretz, 198504 St. Petersburg, Russia

[36] Department of Physics and Astronomy and Space Science Center, University of New Hampshire, Durham, NH 03824, USA

[37] Physics Department and McDonnell Center for the Space Sciences, Washington University in St. Louis, St. Louis, MO 63130, USA

[38] Finnish Centre for Astronomy with ESO, 20014 University of Turku, Finland

[39] Istituto Nazionale di Fisica Nucleare, Sezione di Napoli, Strada Comunale Cinthia, 80126 Napoli, Italy

[40] Université de Strasbourg, CNRS, Observatoire Astronomique de Strasbourg, UMR 7550, 67000 Strasbourg, France

[41] MIT Kavli Institute for Astrophysics and Space Research, Massachusetts Institute of Technology, 77 Massachusetts Avenue, Cambridge, MA 02139, USA

[42] Graduate School of Science, Division of Particle and Astrophysical Science, Nagoya University, Furo-cho, Chikusa-ku, Nagoya, Aichi 464-8602, Japan

[43] Hiroshima Astrophysical Science Center, Hiroshima University, 1-3-1 Kagamiyama, Higashi-Hiroshima, Hiroshima 739-8526, Japan

[44] University of Maryland, Baltimore County, Baltimore, MD 21250, USA

[45] NASA Goddard Space Flight Center, Greenbelt, MD 20771, USA

[46] Center for Research and Exploration in Space Science and Technology, NASA/GSFC, Greenbelt, MD 20771, USA

[47] Department of Physics, University of Hong Kong, Pokfulam, Hong Kong

[48] Department of Astronomy and Astrophysics, Pennsylvania State University, University Park, PA 16801, USA

[49] Center for Astrophysics, Harvard & Smithsonian, 60 Garden St, Cambridge, MA 02138, USA

[50] INAF Osservatorio Astronomico di Brera, via E. Bianchi 46, 23807 Merate (LC), Italy

[51] Dipartimento di Fisica e Astronomia, Università degli Studi di Padova, Via Marzolo 8, 35131 Padova, Italy

[52] Dipartimento di Fisica, Università degli Studi di Roma "Tor Vergata", Via della Ricerca Scientifica 1, 00133 Roma, Italy

[53] Department of Astronomy, University of Maryland, College Park, Maryland 20742, USA

[54] Mullard Space Science Laboratory, University College London, Holmbury St Mary, Dorking, Surrey RH5 6NT, UK

[55] Anton Pannekoek Institute for Astronomy & GRAPPA, University of Amsterdam, Science Park 904, 1098 XH Amsterdam, The Netherlands

[56] Guangxi Key Laboratory for Relativistic Astrophysics, School of Physical Science and Technology, Guangxi University, Nanning 530004, China